Tunable ciprofloxacin delivery through personalized electrospun patches for tympanic membrane perforations

Shivesh Anand [a], Alessandra Fusco [b,c], Cemre Günday [d], Nazende Günday-Türeli [d], Giovanna Donnarumma [b,c], Serena Danti [b,e], Lorenzo Moroni [a], Carlos Mota [a,*]

[a] Department of Complex Tissue Regeneration, MERLN Institute for Technology-Inspired Regenerative Medicine, Maastricht University, 6229 ER, Maastricht, the Netherlands
[b] Interuniversity National Consortiums of Materials Science and Technology (INSTM), 50121, Firenze, Italy
[c] Department of Experimental Medicine, University of Campania "Luigi Vanvitelli", 80138, Naples, Italy
[d] MyBiotech GmbH, Industriestraße 1B, 66802, Uberherrn, Germany
[e] Department of Civil and Industrial Engineering, University of Pisa, 56122, Pisa, Italy

ABSTRACT

Approximately 740 million symptomatic patients are affected by otitis media every year. Being an inflammatory disease affecting the middle ear, it is one of the primary causes of tympanic membrane (TM) perforations, often resulting in impaired hearing abilities. Antibiotic therapy using broad-spectrum fluoroquinolones, such as ciprofloxacin (CIP), is frequently employed and considered the optimal route to treat otitis media. However, patients often get exposed to high dosages to compensate for the low drug concentration reaching the affected site. Therefore, this study aims to integrate tissue engineering with drug delivery strategies to create biomimetic scaffolds promoting TM regeneration while facilitating a localized release of CIP. Distinct electrospinning (ES) modalities were designed in this regard either by blending CIP into the polymer ES solution or by incorporating nanoparticles-based co-ES/electrospraying. The combination of these modalities was investigated as well. A broad range of release kinetic profiles was achieved from the fabricated scaffolds, thereby offering a wide spectrum of antibiotic concentrations that could serve patients with diverse therapeutic needs. Furthermore, the incorporation of CIP into the TM patches demonstrated a favorable influence on their resultant mechanical properties. Biological studies performed with human mesenchymal stromal cells confirmed the absence of any cytotoxic or anti-proliferative effects from the released antibiotic. Finally, antibacterial assays validated the efficacy of CIP-loaded scaffolds in suppressing bacterial infections, highlighting their promising relevance for TM applications.

1. Introduction

Tympanic membrane (TM) is a thin, oval-shaped tissue of the peripheral auditory system, that separates the outer ear from the middle ear cavity. More commonly referred to as the eardrum, the human TM is accredited for the successful transformation of the incoming sound waves into mechanical vibrations. Perforated TM is the most widespread injury to the human ear, often resulting in impaired hearing ability accompanied with tinnitus and vertigo [1]. The leading causes of TM perforations include microbially induced otitis media, along with traumatic accidents such as foreign body instrumentation, explosions and barotrauma [2]. Otitis media is a middle ear inflammatory disease that affects 740 million symptomatic patients every year, with almost 50 % of them occurring in children under 5 years of age [3]. It is, in fact, reported to be the most prevalent reason for medical consultation, antibiotic prescription, and surgical treatment in high-income countries [4–6].

Otitis media can be broadly classified into otitis media with effusion (OME), acute otitis media (AOM), and chronic suppurative otitis media (CSOM) [7]. All the three conditions are characterized by accumulation of a purulent fluid behind the eardrum, which eventually is effused through it by rupturing the tissue. The key difference between OME and

AOM is marked by the apparent signs and symptoms of an acute infection, observed only in case of AOM [8]. On the other hand, CSOM is defined as the chronic inflammation of the middle ear and mastoid cavity, characterized by persistent ear discharge, known as otorrhea, through the perforated TM [9]. Untreated CSOM often leads to conductive hearing loss and poses a risk factor for permanent sensorineural hearing impairment due to inner ear damage, in addition to potential intracranial complications. Overall, it is the leading cause of hearing loss in developing countries [4].

A variety of microorganisms, including aerobic and anaerobic bacteria, have been linked to the onset of otitis media [10]. However, the majority of these reports have indicated a higher occurrence of mono-microbial etiology as opposed to a polymicrobial growth [10]. Furthermore, the bacteriological analysis of CSOM has identified *Staphylococcus aureus* (*S. aureus*) and *Pseudomonas aeruginosa* (*P. aeruginosa*) as the most common pathogens associated with it [11]. The Gram-positive bacterium, *S. aureus*, has shown a higher prevalence

in pediatric cases of CSOM, while the Gram-negative bacterium, *P. aeruginosa* has been more frequently isolated in adults [12]. Antibiotic therapy in the form of systemic or topical administration is frequently employed and considered the optimal route for treating CSOM (Fig. 1A). In this regard, broad-spectrum antibiotics such as second-generation aminoglycosides and quinolones have been applied extensively in the clinics [13,14]. Among them, ciprofloxacin (CIP), an FDA-approved fluoroquinolone, has been found to be particularly effective in inhibiting the microorganism growth, while showing no ototoxicity toward the delicate inner ear [15,16].

In conjunction with the antibiotic treatment, the majority of CSOM-induced TM perforations, especially in adult patients, require an additional medical intervention (known as myringoplasty) to seal the ruptured tissue [17]. Microsurgical placement of autologous grafts derived from temporalis fascia, muscle fascia, cartilage perichondrium, and adipose tissue have been considered as the gold standard for conventional myringoplasty procedures [18]. However, with the growing
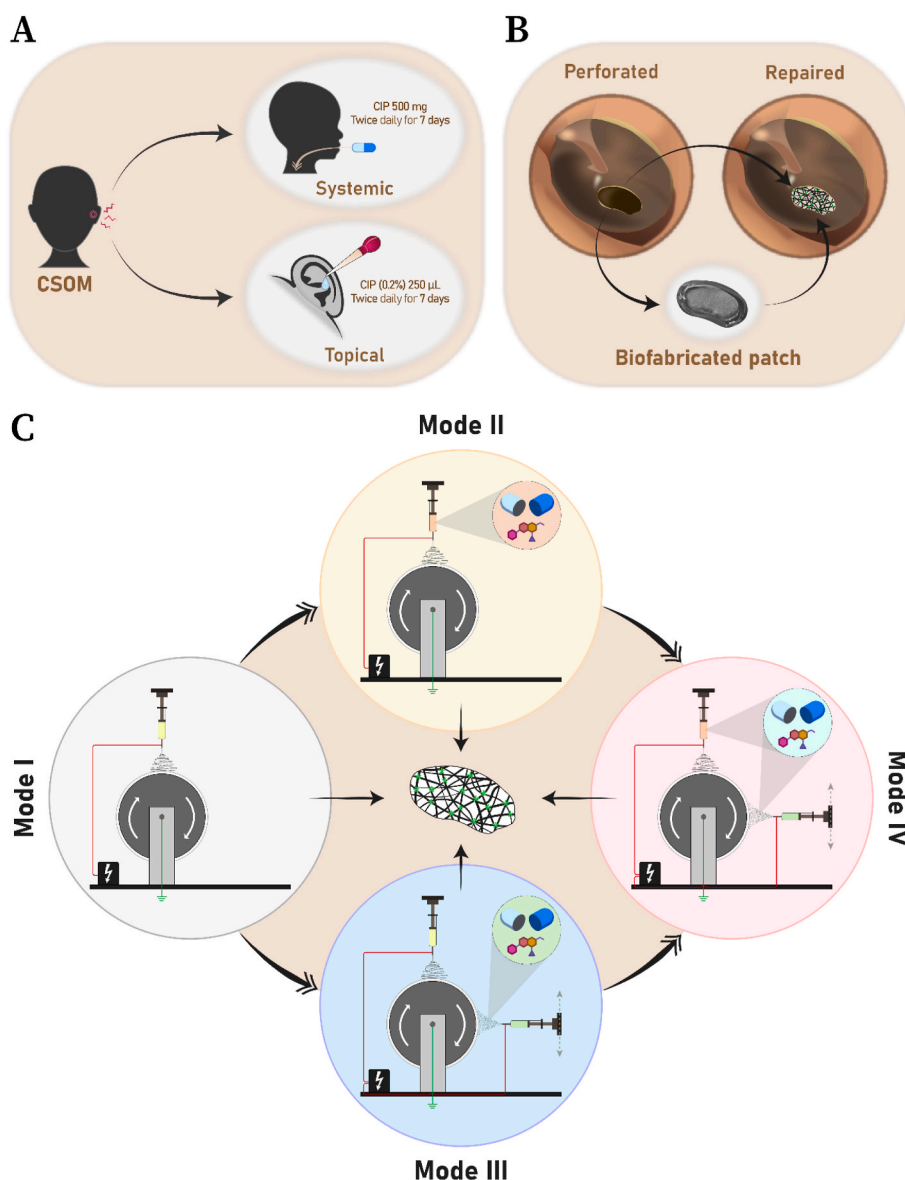
Fig. 1. **(A)** Conventional antibiotic therapies for chronic suppurative otitis media (CSOM). The figure highlights the high concentration of CIP to which the patient is exposed during systemic (1000 mg per day) and topical (1 mg per day) treatments [61,62]. **(B)** Biofabricated patch with antibiotic releasing capabilities. **(C)** Schematic illustration of the distinct electrospinning (ES) modalities investigated in this study. **Mode I:** basic ES with PEOT/PBT (control condition). **Mode II:** blend ES with PEOT/PBT/CIP. **Mode III:** co-ES/electrospraying with PEOT/PBT and PLGA/CIP NPs. **Mode IV:** combination of mode II and III. The arrows represent generation of subsequent modes by suitably adapting the previous one.

prominence of tissue engineering, several biomaterial- and biofabrication-based strategies are being investigated for reconstructing the perforated TM with a superior biological and mechano-acoustical response [19–23]. A wide range of natural and synthetic polymers, spanning from silk fibroin [24,25], alginate [26], gelatin [27,28] to poly (ε-caprolactone) [29–32], and poly(ethylene oxide terephthalate)/poly (butylene terephthalate) (PEOT/PBT) [19,33–36] have been studied for this purpose in combination with biofabrication techniques, such as electrospinning (ES) [19,30–40] and additive manufacturing [19–21,28, 29,33,41,42]. The ability to create nanofibrous electrospun patches with dimensions similar to those of native collagen fibrils in the extracellular matrix [43] supports ES as a promising approach for reconstructing CSOM-induced TM injuries using tissue-engineered scaffolds.

Moreover, in the recent years, electrospun meshes have emerged as versatile carriers for numerous bioactive compounds, serving various drug delivery applications [44]. The flexibility offered by ES in terms of material selection, drug loading methodologies, and drug release mechanisms enables precise control over the resulting release kinetics of the loaded drug [45]. Multiple ES modalities have been investigated for incorporating a vast spectrum of drugs, extending from antibiotics [46] and anticancer medications [47] to proteins [48], DNA [49], and RNA [50]. Among them, some of the key approaches including blend ES [51], co-ES/electrospraying [52], side-by-side ES [53], co-axial ES [54], and emulsion ES [55], have also been applied for the inclusion of CIP. The diverse loading methodologies allow the creation of electrospun scaffolds with the specific antibiotic content and release profile required for the intended application.

In this regard, blend ES has been noted to be particularly successful in achieving a sustained CIP release over an extended period of time [56–58]. The approach involves blending the drug directly into the precursor polymeric solution, thereby entrapping CIP within the resultant electrospun fibers. Such a physical entrapment of the drug usually facilitates its long-term release, governed by the swelling, diffusion, and degradation rates of the surrounding polymer [59]. However, in many cases, a direct dependence on the polymer properties is not desirable, especially if it demands composition changes affecting the mechanical or biological response of the corresponding scaffolds. A promising alternative to circumvent this issue has been the surface functionalization of electrospun fibers using drug-loaded nanoparticles (NP) [60]. The recent work of Günday et al. demonstrated an innovative approach in this direction, where a co-ES/electrospraying technique was employed for the simultaneous deposition of PEOT/PBT nanofibers along with CIP-encapsulated poly(D,L-lactide-*co*-glycolide) (PLGA) NP [52]. Considering the growing relevance of PEOT/PBT scaffolds for TM regeneration [19,33–36], the proof-of-concept highlighted by Günday et al. presented a favorable strategy for the CSOM treatment. Yet, the current literature lacks tissue engineering therapies precisely designed for the potential restoration of microbially induced TM perforations through targeted antibiotic delivery.

Therefore, this work aims to fill the existing gap in the creation of TM patches with tunable drug releasing capabilities (Fig. 1B). Distinct ES modalities were applied to fabricate CIP-loaded PEOT/PBT patches and provide a versatile platform for diverse therapeutic needs (Fig. 1C). In the first modality, referred to as mode I, a conventional single-jet setup was established to produce blank electrospun patches for TM injuries that do not require antibiotic treatment. Modes II, III, and IV were subsequently developed specifically for complex CSOM cases, necessitating varying degrees of antibiotic treatment. This was obtained via blend ES in mode II, co-ES/electrospraying in mode III, and a combination of the two in mode IV. A parametric investigation in terms of surface morphology, physicochemical properties, drug release kinetics, and mechanical response was performed for each ES modality to determine their respective CIP loading capacity. In this regard, the blend ES was optimized with respect to the CIP concentration and the co-ES/ electrospraying with the NP flow rate. The following *in vitro* assessments were conducted on the optimal TM scaffolds identified for each of the

four ES modes. Ultimately, antibacterial assays were conducted to validate the tunable CIP release achieved through the distinct fabrication strategies.

2. Materials and methods

2.1. Materials

The 300PEOT55PBT45 grade of PEOT/PBT copolymer (kindly provided by PolyVation B.V., the Netherlands) was used as the suitable biomaterial for fabricating the TM scaffolds. Following an *a*PEOT*b*PBT*c* nomenclature, the 300 (*a*) denotes molecular weight (*Mw*, g/mol) of the initial polyethylene glycol blocks during copolymerization, whereas 55/ 45 (*b/c*) represents the weight ratio of PEOT and PBT, respectively. The commercial polymer was purified by repeated dissolution in trichloromethane (anhydrous, Sigma-Aldrich, the Netherlands) and precipitation in absolute ethanol (VWR International B.V., the Netherlands) (Figure S1A). The purification of PEOT/PBT was confirmed by immersing the polymer in Dulbecco's phosphate-buffered saline (DPBS, Sigma-Aldrich, the Netherlands) and recording the ultraviolet–visible spectra (UV–vis; Agilent Cary 60, USA) of the eluent over a period of 10 days (Figure S1B). Thereafter the purified PEOT/PBT was employed for the fabrication and all subsequent characterizations. The ES precursor solution was prepared based on prior studies in literature [19,52], where the copolymer was dissolved in a 70:30 (*v/v*) solvent mixture of trichloromethane and hexafluoro-2-propanol (HFIP, analytical reagent grade, Biosolve B.V., the Netherlands) through overnight stirring at ambient temperature (Figure S2A).

CIP (Sigma-Aldrich, the Netherlands) was employed as the clinically relevant antibiotic for the creation of TM patches. For blend ES (modes II and IV), the CIP was pre-dissolved in the trichloromethane/HFIP solvent mixture by ultrasonication (US) at 37 °C for 30 min (Branson 5800-E, the Netherlands). Following the overnight stirring with PEOT/PBT, two distinct approaches were tested to prepare a homogeneous precursor solution for mode II. The first one (US+) included an additional ultrasonication step at 37 °C for 30 min right before ES, whereas the second approach (US-) did not comprise any further ultrasonication. On the other hand, for co-ES/electrospraying (modes III and IV), nanoprecipitation-based PLGA NP were prepared using continuous microreactor technology [52].

2.2. Preparation of PLGA NP

Blank PLGA and CIP-loaded PLGA NP (PLGA/CIP NP) were prepared by employing the nanoprecipitation methodology, as previously described by Günday et al. [52]. In brief, the solvent system (consisting of 0.4 % (*w/v*) PLGA and 0.15 % (*w/v*) Span 80® solution in acetone, mixed with 4.85 % CIP solution in oleic acid) and the non-solvent system (0.15 % (*w/v*) aqueous Tween 80 solution) were nanoprecipitated continuously at a 1:2 ratio and an angle of 180° under ambient conditions. In case of the labelled NP preparation, 1.12×10^{-4} % (*w/v*) Lumogen F Red 305® (BASF, Germany) was introduced into the solvent system. The purification process, involving the removal of free formulation components and organic solvent, as well as the concentration of the formulation to achieve the desired CIP concentration, was achieved through continuous flow filtration using modified polyethersulfone MidiKros® hollow fiber filters (MWCO: 10 kDa, surface area: 235 cm²; Spectrum, Repligen Europe B.V., Netherlands).

2.3. Fabrication of electrospun TM patches

Different ES modalities were applied for the fabrication of biomimetic patches for CSOM-induced TM perforations. Initially, a conventional single-jet setup (mode I) was established on the Fluidnatek LE–100 (Bioinicia S.L., Spain), and thereafter, necessary adjustments were made to obtain the subsequent modes. The same single-jet

configuration was employed for mode II as well, where PEOT/PBT/CIP blend was electrospun instead of the standard PEOT/PBT precursor solution. In case of modes III and IV, a dual-jet setup was implemented to simultaneously electrospray CIP-loaded PLGA NP during ES. The two spinnerets were placed perpendicular to each other to avoid electrostatic interaction between the jets.

The operating parameters for ES were selected based on the previously conducted optimization for fabricating functional TM scaffolds [19]. Identical values were used with respect to the PEOT/PBT concentration (17 % *w/v*), polymer flow rate (0.9 mL h^{-1}), air gap (10 cm), collector rotation (200 revolutions per minute), spinneret diameter (0.8 mm), and environmental conditions (23 °C temperature and 40 % relative humidity). However, the applied voltage was adjusted to 14 kV (spinneret = 11 kV; collected = −3 kV) to ensure a stable Taylor's cone for the PEOT/PBT/CIP blend solutions. Four different CIP concentrations were investigated within the mode II: 2.5 %, 5.0 %, 10.0 %, and 20.0 % (*w/w* with respect to PEOT/PBT).

Additional parameters in terms of flow rate and air gap were included for the simultaneous electrospraying of the NP suspension. In this regard, the PLGA/CIP NP were kept consistent with respect to the previously optimized size (Figure S2B) and concentration, while their loading volume was varied. Three distinct flow rates were evaluated: 1.5 mL h^{-1}, 3.0 mL h^{-1}, and 6.0 mL h^{-1}; whereas the air gap was maintained consistent at 5 cm. Finally, the mode IV scaffolds were fabricated using a polymeric solution containing 2.5 % CIP, combined with a flow rate of 3.0 mL h^{-1} for the PLGA/CIP NP suspension. All the electrospun meshes were collected on a cylindrical mandrel (stainless steel, diameter = 200 mm, length = 300 mm) wrapped with an aluminum substrate comprising circular bands (inner diameter = 12 mm, outer diameter = 15 mm) of Finishmat 6691 LL (Lantor B.V., the Netherlands). These supporting bands were used to allow an easy handling of the TM scaffolds for the subsequent characterizations. An ES duration of 35 min was executed for all the modalities.

After punching out the electrospun meshes, a pre-washing step was performed for disinfecting the samples and to facilitate the removal of the aluminum substrate. Depending on the ES modality, two different approaches were implemented for this purpose. In the first approach, which was applied for mode I and II, samples were immersed in 70 % ethanol (VWR International B.V., the Netherlands) for 5 min. Whereas the mode III and IV scaffolds were disinfected by immersing them in DPBS and exposing to UV radiation at 40 mJ cm^2 for 5 min.

2.4. Wet ES

The wet electrospinning experiments were carried out by substituting the rotating collector with a glass Petri dish wrapped in aluminum foil. Three distinct solvents: water, ethanol, and isopropanol, were successively used as a collecting substrate within the conductive Petri dish. An identical set of parameters, including polymer concentration, flow rate, applied voltage, air gap, and environmental conditions, was applied during the collection of the PEOT/PBT solution.

2.5. Morphological characterization

Scanning electron microscopy (SEM) was performed to examine the nanofiber morphology (top view) and thickness (cross-sectional view) of the electrospun meshes. A thin layer of gold coating was applied (Quorum Technologies SC7620, UK) over the samples before imaging on the microscope (Jeol JSM-IT200, the Netherlands). The images were captured at 3000× magnification, with an accelerating voltage of 10 kV and working distance of 10 mm. The subsequent image processing and analysis was performed on Fiji software (version 2.9.0, https://fiji.sc/) to determine fiber diameter (*n = 3 samples × 25 measurements each*) and thickness (*n = 3 samples × 4 measurements each*) of the scaffolds.

2.6. Physicochemical characterization

The physicochemical characterization of the mode II electrospun meshes was conducted by carrying out Fourier transform infrared spectroscopy (FTIR), X-ray diffraction analysis (XRD), and water contact angle measurement (WCA). The chemical composition of the samples was analyzed using attenuated total reflection FTIR (Nicolet™ iS50, Thermo Fisher Scientific, the Netherlands) in the range of 400–4000 cm^{-1} with a resolution of 0.5 cm^{-1}. The crystallinity of the fabricated scaffolds was assessed with XRD (Bruker D2 Phaser, the Netherlands). X-ray diffractograms were collected using Cu Kα radiation ($\lambda = 1.5406$ Å) between $5° \leq 2\theta \leq 70°$ in increments of 0.02°. The sample wettability was assessed by WCA. A drop shape analyzer (Krüss DSA25S, Germany) was used to deposit sessile water droplets with a volume of 4 μL. The resultant contact angles (right and left) formed by the droplets on the surface were calculated by applying Laplace-Young computational method. Finally, to evaluate the wettability speed, measurements were performed until the water droplet was fully dispersed within the electrospun meshes.

The NP suspensions employed for creating mode III and IV electrospun meshes was characterized using dynamic lighting scattering (DLS). Particle size and polydispersity index of the CIP-loaded and blank NP suspensions were measured on a DLS zetasizer (Malvern Instruments Nano ZSP, UK) in disposable cuvettes (BRAND® macro, Sigma-Aldrich, the Netherlands) containing 1000 μL of the sample. The successful adhesion of the electrosprayed NP on electrospun nanofibers was confirmed by synthesizing Lumogen Red F305 labelled PLGA/CIP NP. The Lumogen dye was specifically chelated to PLGA through its ester bonds; therefore, any fluorescent signal detected upon placing the electrospun scaffold in DPBS indicated a poor attachment of the NP. The release of non-adhering NP was quantified over a period of 7 days using a multi-mode plate reader (CLARIOstar, BMG LABTECH, Germany). This was investigated for mode III samples in comparison to the previously reported immersion approach (negative control) [52].

2.7. Drug release kinetics

The release kinetics of CIP was evaluated for all the ES modes at 37 °C. Samples were placed in a 24-well plate (non-treated, 734–0949, VWR International B.V., the Netherlands) held by O-rings (FKM 75 51414, 11.89 × 1.98 mm, ERIKS N.V., the Netherlands). Pre-warmed DPBS was used as the suitable eluent solution, where a volume of 1000 μL was pipetted onto each electrospun scaffold. The antibiotic release was investigated by withdrawing 100 μL of the eluent at each timepoint, which was then replaced with fresh, pre-warmed DPBS of an equal volume. The study was carried out for a total duration of 7 days, with measurements obtained at the following timepoints: 1 h, 6 h, 12 h, 24 h, 48 h, 72 h, 120 h, and 168 h. The drug concentration in the collected sample was determined based on absorbance values of CIP recorded by the UV–vis spectrophotometer. All UV–vis measurements were performed in a 50 μL quartz cuvette (Hellma 105-202-85-40, Belgium) at ambient temperature. A wavelength range of 500 nm–200 nm with a step size of 0.5 nm was chosen to register all the characteristic peaks of CIP (Figure S4A). A standard curve for CIP was generated in the respective solvents, which was thereafter used for all the concentration calculations (Figure S4B-C).

An anti-evaporation lid was developed to prevent any eluent loss while storing the samples for a span of 7 days at 37 °C (Figure S4D). For this, a bicomponent silicone rubber (Zhermack HT 45 Transparent, Italy) was molded into a negative replica of the standard 24-well plates and used as a sealant to prevent evaporation.

2.8. Mechanical characterization

Tensile and macroindentation measurements were performed on the fabricated electrospun patches to evaluate their mechanical response

(Figure S5). The test benches for both measurements were configured using previously reported protocols and operating parameters [19]. In brief, the analysis was conducted on a uniaxial mechanical tester (TA ElectroForce 3200, USA) at ambient temperature. All samples were evaluated under dry conditions until the point of rupture.

Tensile tests were performed to characterize the different scaffold compositions of mode II (PEOT/PBT/CIP 2.5 %, 5.0 %, 10.0 %, and 20.0 %) and mode III (flow rate of 1.5 mL·h^{-1}, 3.0 mL·h^{-1}, and 6.0 mL·h^{-1}). The sample preparation was maintained consistent throughout all the tested conditions; however, small variations in the geometrical dimensions (length, width, and thickness) were duly registered before each test. The length and width were measured with a digital caliper, whereas the thickness was quantified from SEM micrographs of the cross-sectional view. A 45 N load cell was used with a scan rate of v mm·s^{-1}, where v represents the speed at which a displacement equivalent to 0.5 % of the sample length (in mm) is covered in 1 s. Finally, individual stress-strain curves were computed for each sample with respect to their exact dimensional properties.

Subsequently, the macroindentation measurement, which is a relevant technique for characterizing the TM functionality, was performed for the best composition chosen per ES modality. Based on the nanofibrous morphology and drug release kinetics, CIP 10.0 % and flow rate of 1.5 mL·h^{-1} were identified as the most optimal conditions for mode II and III, respectively. An identical scan rate as the tensile tests were applied in combination with a 10 N load cell. The stress-strain curves were computed by approximating a pure stretching behavior between the applied load and the outer sample boundary [19].

2.9. Biological characterization

Human mesenchymal stromal cells (hMSCs) were used to assess the biological response of the fabricated electrospun patches. Following ethical approval from the local and national authorities, the cells were isolated from the iliac crest (Donor 064, male, age 17, Maastricht University Medical Center, Maastricht, the Netherlands). All procedures were carried out in accordance with the World Medical Association Declaration of Helsinki in its latest amendment. The isolated hMSCs were cultured in α-minimal essential medium with Glutamax (α-MEM; no nucleosides, Fisher Scientific, the Netherlands) supplemented with 10 % heat-inactivated fetal bovine serum (FBS; Sigma-Aldrich, the Netherlands) and 1 % penicillin/streptomycin (PS; 100 U·mL^{-1}, Thermo Fisher Scientific, the Netherlands).

The scaffolds were disinfected as described previously, after which they were placed in 24-well plates and held by sterile O-rings. A seeding density corresponding to 100,000 cells per scaffold was deposited dropwise on the sample surface. Treated tissue culture plate (TCP) was employed as control. The seeded hMSCs were cultured for a duration of 7 days, with three specific time-points (day 1, 3, and 7) chosen for the subsequent characterizations. During the process, the culture media was refreshed every 3 days using conditioned medium, prepared by incubating unseeded acellular replicates of the respective samples under identical conditions (37 °C, 5 % CO$_2$). Finally, the following assays were performed at each time-point to evaluate the influence of ES modality on hMSC viability, attachment, and proliferation:

Live cell staining and imaging: Cultured scaffolds were washed with DPBS and incubated with 0.025 % (v/v) of Calcein AM (Thermo Fisher Scientific, the Netherlands) for 30 min at 37 °C. Microscopy imaging of the live cells was performed on an inverted microscope (Nikon Eclipse Ti-E, the Netherlands), equipped with an incubator (Okolab, Italy).

Cell metabolic activity: The enzymatic reduction of MTS tetrazolium compound (Abcam, UK) to colored formazan product was utilized for quantifying the metabolically active cells. As per the manufacturer's protocol, the MTS reagent was added directly to the culture media in a 1:11 (v/v) ratio, and incubated for 4 h at 37 °C. After the incubation period, samples were collected in a 96-well plate (standard, VWR International B.V., the Netherlands) and absorbance measured at an optical density (O.D.) of 490 nm in the plate reader.

dsDNA quantification: Cultured scaffolds were washed with DPBS and incubated in 1 mL of ultrapure water for 1 h at 37 °C. Thereafter, the samples were subjected to a freeze/thaw cycle at −80 °C/ambient temperature to induce cell lysis. The DNA quantification was performed using Quant-iT™ PicoGreen™ dsDNA assay (Invitrogen™, Thermo Fisher Scientific, the Netherlands) following the manufacturer's instructions.

Immunostaining and imaging: All incubation steps during staining were carried out at ambient temperature, unless specified otherwise. Cultured scaffolds were washed with DPBS and fixed with 3.7 % (v/v) formaldehyde solution (ACS reagent, Sigma-Aldrich, the Netherlands) for 30 min. Fixed samples were treated with 0.1 % (w/v) Sudan Black B dye (in 70 % ethanol; Sigma-Aldrich, the Netherlands) for 45 min. Thereafter, they were incubated with 0.1 % Triton™ X-100 (in DPBS; Sigma-Aldrich, the Netherlands) for 10 min, followed by 1 % bovine serum albumin (in DPBS; VWR Chemicals, the Netherlands) for 1 h. Finally, the permeabilized and blocked cells were stained with Alexa Fluor® 647 Mouse anti-Ki-67 (1:25 in DPBS (v/v); BD Bioscience, the Netherlands) overnight at 4 °C, Alexa Fluor 488 phalloidin (1:100 in DPBS (v/v); Thermo Fisher Scientific, the Netherlands) for 45 min, and 4,6-diamideino-2-phenylindole dihydrochloride (DAPI; 1:1000 in DPBS (v/v); Sigma-Aldrich, the Netherlands) for 20 min. Fluorescence images were acquired using the inverted microscope as described previously.

2.10. Antibacterial characterization

S. aureus (ATCC® 6538™, USA) and *P. aeruginosa* (ATCC® 9027™, USA) were cultured in Bacto Tryptic Soy Broth (TSB; Difco Laboratories, USA) at 37 °C for 18 h. Subsequently, the cultures were diluted at a concentration of 0.5 O.D., and 100 μL of each was plated on agar medium (Sigma-Aldrich, the Netherlands) with the help of a swab. Following sowing, the sterilized mode I, II, III, and IV samples were applied on the surface of the agar plates and the bacteria were incubated overnight at 37 °C. The antibacterial activity was revealed by the presence of a transparent zone around the samples, due to the inhibition of microbial growth. The assays were carried out in triplicate for each species and each sample.

For the biofilm assessment, overnight cultures of *S. aureus* and *P. aeruginosa* were diluted with Oxoid™ Gamma-Irradiated TSB (Thermo Fisher Scientific, the Netherlands), as positive control to obtain a concentration of 107 CFUs per mL. Sterilized mode I, II, III, and IV meshes were placed into 96-well flat-bottomed sterile polystyrene microplates (Costar, Corning Inc., USA). Thereafter, 200 μL aliquots of the diluted bacterial suspension were dispensed into the wells containing the samples and incubated overnight at 37 °C in aerobic conditions. The biofilm formation was then evaluated by SEM analysis.

For the quantification of biofilm formation, sterilized mode I, II, III, and IV meshes were placed into 96-well flat-bottom polystyrene microplates (Costar, Corning Inc. USA). Thereafter, 200 μL aliquots of the diluted overnight bacterial suspension of S. aureus and P. aeruginosa were dispensed into the wells containing the samples and incubated overnight at 37 °C in aerobic conditions. As positive control, bacteria adhered on the bottom of the well was used. The biofilm formed was quantified by a modified crystal violet assay [63]. Briefly, after 2, 4, 6 and 24 h, the attached bacteria were washed twice with 200 μL of PBS and air-dried for 45 min. The meshes on the bottom of the wells were then stained with 200 μL of 0.5 % (w/v) aqueous crystal violet solution for 45 min, rinsed with 200 μL of sterile distilled water to remove excess dye and air-dried. The dye associated with attached biofilm was dissolved in a solution of 200 μL of absolute ethanol, and the OD$_{570/655}$ absorbance was measured with a microplate reader.

2.11. Statistical analysis

The samples were assigned randomly to different experimental groups, and the number of replicates (*n*) for each experiment have been specified in the figure captions. Statistical analysis was performed using GraphPad Prism 8 (GraphPad Software, USA), where the statistical significance was determined by applying a one-way or two-way analysis of variance (ANOVA) followed by a Tukey's honestly significant
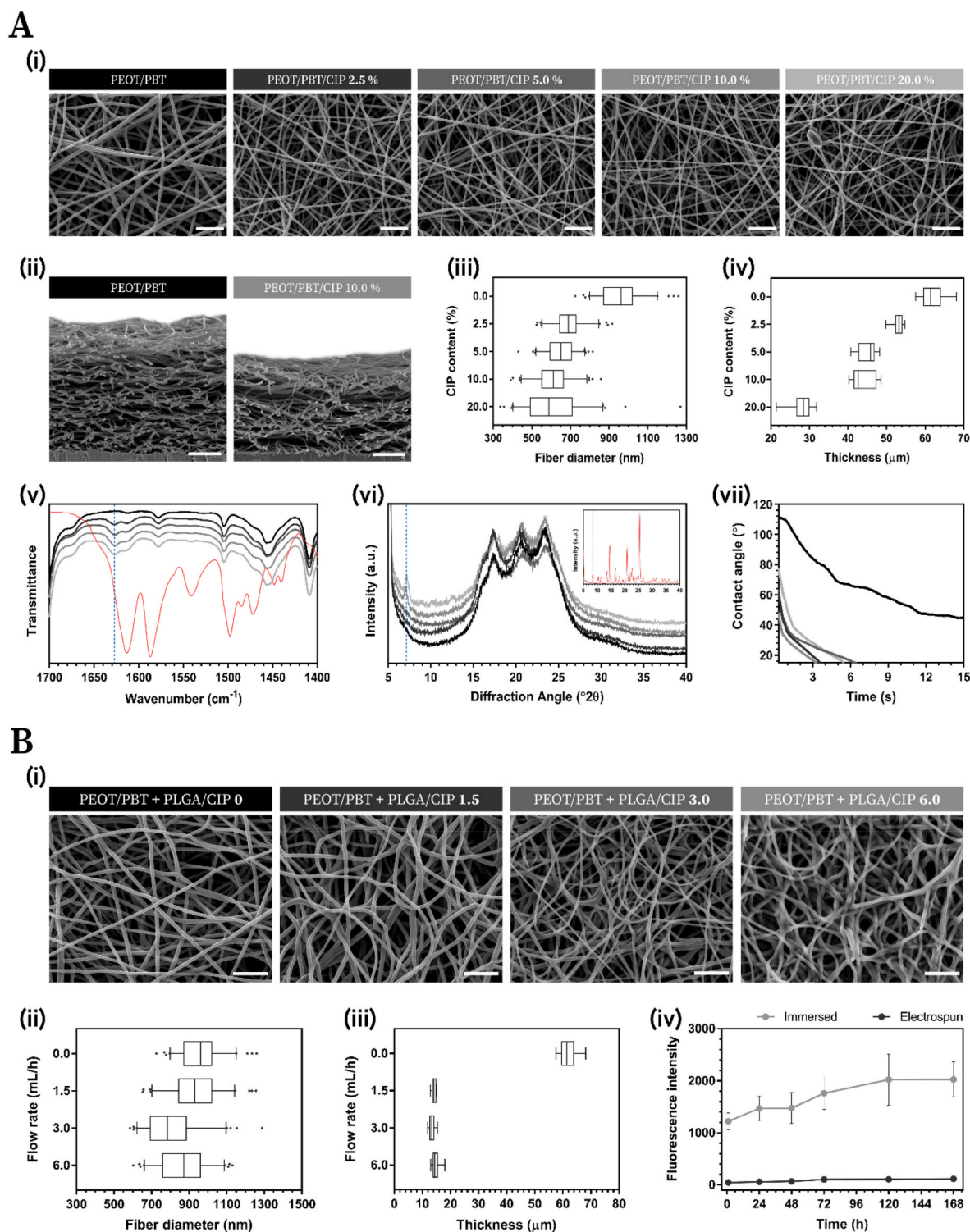
Fig. 2. Morphological and physicochemical characterization of the electrospun patches. (A) Mode II: (i) Scanning electron micrographs of blend electrospun scaffolds fabricated with different CIP content. **(ii)** Cross-sectional view of the meshes. **(iii)** Quantification of the nanofiber diameter (*n* = 75). **(iv)** Thickness quantification of the meshes (*n* = 12). **(v)** Fourier-transform infrared spectra of the meshes with respect to CIP (red), and **(vi)** X-ray diffraction spectra of the fabricated scaffolds along with CIP in inset. **(vii)** Water contact angle measurements. **(B) Mode III: (i)** Scanning electron micrographs of co-electrospun/electrosprayed scaffolds. **(ii)** Quantification of the nanofiber diameter (*n* = 75). **(iii)** Thickness quantification of the meshes (*n* = 12). **(iv)** Adhesion of the nanoparticles confirmed by the low release of Lumogen Red F305 dye.

difference (HSD) post-hoc test. Data are given as mean $\pm$ standard deviation, with probability (p) levels: with $*p < 0.05$, $**p < 0.01$, $***p < 0.005$, $****p < 0.0001$, and $p > 0.05$ not significant (*ns*).

3. Results

3.1. Morphological and physicochemical characterization

The successful incorporation of CIP within the fabricated electrospun meshes was demonstrated through various morphological and physicochemical characterizations. Considering the differences in the loading mechanism and their resultant drug content, distinct analytic techniques were applied to characterize the chosen ES modalities. These results have been summarized for blend ES in Fig. 2A and for co-ES/electrospraying in Fig. 2B.

A significant reduction in the electrospun fiber diameter and cross-sectional thickness was obtained with the inclusion of CIP in the polymeric blend (Fig. 2A (i)–(ii)). Moreover, as the CIP concentration was increased, a gradual decrement in both these morphological properties was observed (Fig. 2A (iii)–(iv)). In case of fiber diameter, this trend was achieved up to CIP 10.0 %, beyond which the ES jet turned unstable and resulted in erratic bead formation. The substantially high standard deviation for CIP 20.0 % validated its inconsistent fiber distribution (Fig. 2A (iii)). A similar outcome was also detected for the thickness measurements, with CIP concentrations of 2.5 %, 5.0 %, and 10.0 % showing comparable results, in contrast to the drastic reduction obtained with CIP 20.0 % (Fig. 2A (iv)).

Physicochemical characterizations, including FTIR, XRD, and WCA, were conducted to confirm that the morphological differences identified between the investigated compositions was due to the presence of CIP. FTIR spectra of the mode II scaffolds revealed appearance of new absorption peaks that were not present in the pristine PEOT/PBT fibers of mode I (Fig. 2A (v)). Upon comparison with commercial CIP powder, the observed bands were assigned to the characteristic N–H bending (1627 cm^{-1}) and N–H wagging (683 cm^{-1}) of the amine groups in CIP (Figure S2B). Moreover, a blue shift towards higher wavenumbers was recorded across all the electrospun samples, which could be attributed to a stronger molecular interaction within the polymeric network in contrast to the CIP powder. The XRD spectra of all PEOT/PBT/CIP scaffolds demonstrated an identical semi-crystalline structure as that of the pristine PEOT/PBT (Fig. 2A (vi)). On the contrary, a highly crystalline structure was noted for the pristine CIP (inset, Fig. 2A (vi)). These results confirmed the molecular integration of CIP within the polymeric nanofibers, where its characteristic peak (7.15°) was detected only at higher drug concentrations (10.0 % and 20.0 %). The WCA measurements of all the PEOT/PBT/CIP meshes revealed a significantly faster dispersion of water in comparison to the pristine PEOT/PBT nanofibers (Fig. 2A (vii)). As a result, the addition of CIP to the electrospun meshes presented a favorable influence on their hydrophilicity, irrespective of the encapsulation amount.

A morphological characterization of the co-electrospun/electrosprayed meshes was performed to evaluate the influence of NP flow rate on the fiber collection (Fig. 2B (i)–(iii)). Qualitative assessment of the resultant nanofibers revealed a curlier morphology in the scaffolds electrosprayed with NP (at 1.5 mL·h^{-1}, 3.0 mL·h^{-1}, and 6.0 mL·h^{-1}) as compared to their non-electrosprayed counterparts (0 mL·h^{-1}) (Fig. 2B (i)). This was further investigated by implementing the technique of wet ES as a positive control, where three distinct collecting solvents: water, ethanol, and isopropanol, were used to understand the relationship between the collector's surface tension and the corresponding fiber morphology (Figure S3B). SEM micrographs of the subsequent PEOT/PBT nanofibers revealed an increment in the curling effect as the surface tension of the collector was lowered from 71.1 mN·m^{-1} to 20.5 mN·m^{-1} [64]. The quantitative assessment in terms of the scaffold thickness also displayed a significant impact of simultaneous electrospraying on the collection efficiency (Fig. 2B (iii)). However, the fiber diameter

remained consistent across all conditions (Fig. 2B (ii)). Finally, the adhesion of the electrosprayed NP was confirmed in comparison to the negative control samples prepared by immersion technique (Fig. 2B (iv)).

3.2. Drug release kinetics

The drug release kinetics of CIP-loaded electrospun patches were evaluated envisioning their potential application on CSOM-induced TM perforations. In this view, a sustained delivery of the antibiotic is essential for limiting the proliferation of the responsible pathogens, as well as for preventing chances of reinfection. The exact duration of the antibiotic therapy is largely dependent on patient's medical history and the administered dose [65,66]. Therefore, fabrication of TM patches with tunable drug releasing capabilities was investigated.
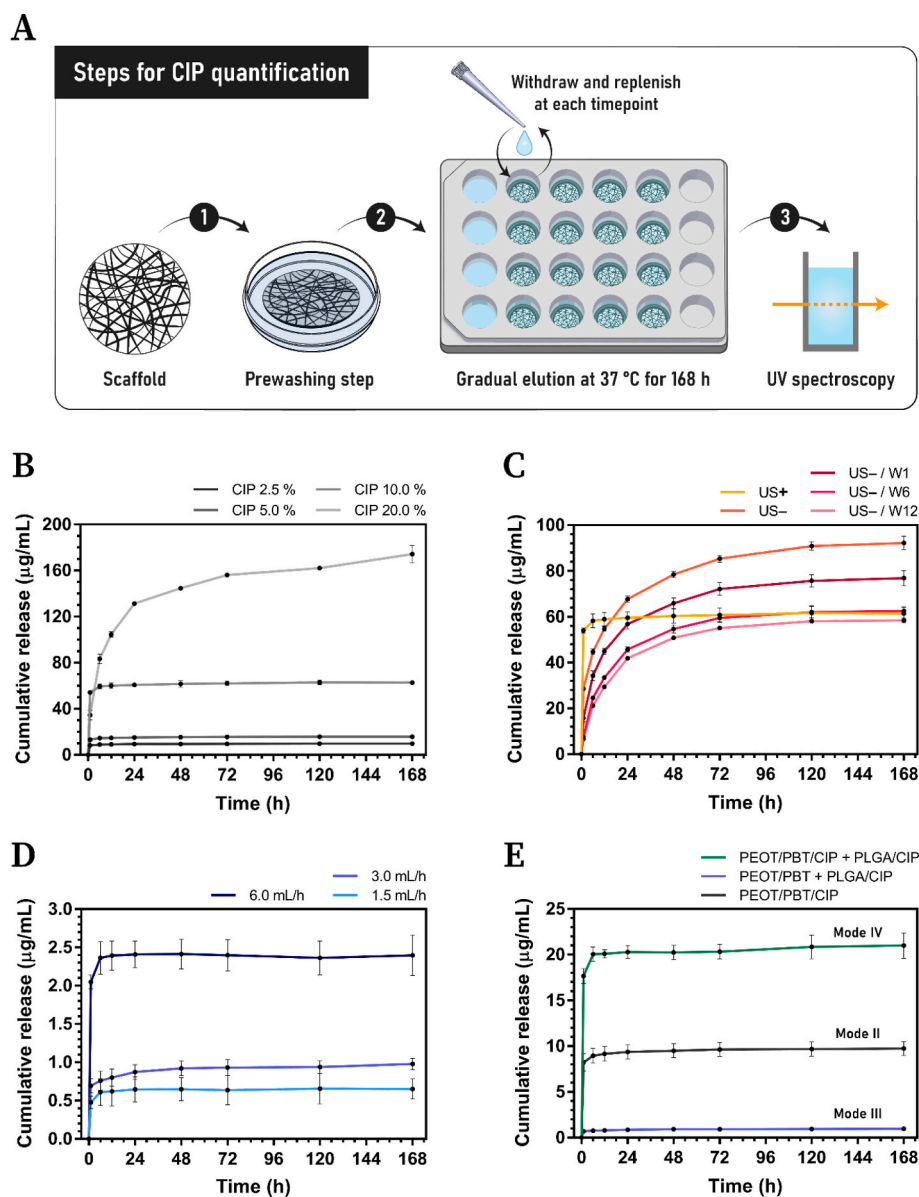
Fig. 3A illustrates a schematic representation of the implemented release kinetic study. The cumulative release of CIP from the fabricated scaffolds was examined over a period of 7 days. The resultant curves have been summarized in Fig. 3B–C for mode II, Fig. 3D for mode III, and Fig. 3E for mode IV. To understand the influence of drug solubility and dispersion, the mode II samples were prepared both with (US+) and without (US-) an additional ultrasonication step. Visually, the subsequent ultrasonication allowed the creation of a distinctly clearer precursor solution as compared to the blends that were not ultrasonicated prior to ES. This behavior was specifically observed for CIP concentrations $\geq$10.0 %, where the absence of the final ultrasonication step led to a murky and less translucent solution. However, the transparency obtained in case of US + samples presented an adverse effect on the desired release profile of CIP. In this regard, all the compositions except for CIP 20.0 % showed a burst release, with a substantial amount of the loaded drug being let out within the first 6 h (Fig. 3B). On the contrary, when tested without the additional ultrasonication step (US-), the CIP 10.0 % exhibited a sustained response as well (Fig. 3C). Furthermore, to regulate the cumulative concentration achieved by the US- scaffolds, an additional washing step of 1 h, 6 h, or 12 h was introduced prior to the release study. This step was essential to reduce the drug concentration in accordance with the reported half maximal inhibitory concentration (IC$_{50}$ = 50 μg·mL^{-1}) and the ninety percent inhibitory concentration (IC$_{90}$ = 253 μg·mL^{-1}) for the anti-proliferative activity of CIP on hMSCs [67]. Based on these results, PEOT/PBT/CIP 10.0 % fabricated without ultrasonication followed by a 12 h washing step, was chosen as the optimal condition among all the mode II formulations.

In the case of mode III, an increase in CIP concentration was observed with the rising flow rates, which could be attributed to the higher number of drug-loaded NP deposited with faster flow rates (Fig. 3D). Overall, a burst release was noted for all the conditions across a 7-day timescale. Among them, the flow rate of 3.0 mL·h^{-1} demonstrated the most controlled release, displaying gradual increments over a period of 48 h. Thus, it was chosen as the optimal parameter for mode III and subsequently applied to mode IV. In addition, a CIP concentration of 2.5 % was used for the blend ES component of the mode IV. Analogous to their constituent counterparts in modes II and III, the resulting scaffolds exhibited an initial burst of drug release (Fig. 3E). Moreover, a significantly higher cumulative concentration was achieved with mode IV, despite employing the same CIP content. This enhancement can be attributed to reduced drug losses during the disinfection step in DPBS using UV radiation compared to that in ethanol (Figure S4A).

3.3. Mechanical characterization

The successful conversion of acoustical waves into mechanical motion of the TM is accredited to the unique properties of its extracellular matrix. Therefore, replicating this precise mechanical response in a therapeutic TM patch is essential to potentially restore the patient's full hearing capacity [68]. On that account, a thorough mechanical characterization was performed for all the ES modalities investigated in this

Fig. 3. Release kinetics of CIP from the electrospun patches. (A) Schematic representation of the drug release experiments. **(B)** PEOT/PBT/CIP blend electrospun scaffolds (mode II) fabricated with the ultrasonication step (US+); $n = 3$. **(C)** PEOT/PBT/CIP 10 % (mode II) repeated with no ultrasonication (US-) and washing step (W); $n = 4$. **(D)** PEOT/PBT + PLGA/CIP co-electrospun/electrosprayed scaffolds (mode III); $n = 3$. **(E)** Scaffolds fabricated by combining blend electrospinning with co-electrospinning/electrospraying (mode IV); $n = 6$. A CIP concentration of 2.5 % was applied in combination with a NP flow rate of 3.0 mL·h^{-1}.

study. Tensile tests were conducted for the different compositions of mode II and III (Fig. 4A), which was followed by macroindentation measurements of the most optimal condition chosen for each modality (Fig. 4B).

In general, the addition of CIP enhanced the mechanical properties of the resultant scaffolds. A gradual increment in the stress-strain profiles was noticed with rising CIP content in the mode II blends (Fig. 4A (i)). This was verified within the linear elastic regime as well, where a progressive rise in the Young's modulus (E) was obtained across the tested samples (left to right bars, Fig. 4A (ii)). Among them, CIP 20.0 % demonstrated a significantly higher E value, while on the contrary, no statistical differences were revealed between the remaining mode II compositions. A similar trend was also observed in case of mode III, where the simultaneous electrospraying of CIP-loaded NP resulted in mechanically stiffer scaffolds as compared to the pristine PEOT/PBT meshes of Mode I (Fig. 4A (iii)). Furthermore, as the NP flow rate rose, a subsequent increase in the corresponding E values was recorded (Fig. 4A

(iv)). To conclude, the tensile measurements indicated mode I to have the lowest mechanical properties with an $E = 2.72$ MPa, which was followed by mode II with average E values in the range of 3.24–4.99 MPa depending on the CIP concentration and ultimately mode III with average E values lying between 8.01 and 9.84 MPa.

Subsequently, the obtained results were corroborated by implementing a previously reported macroindentation approach [19,36]. The study was carried out by identifying the most relevant composition for each mode, determined based on the characterizations performed so far. In this regard, CIP 10.0 % was selected for mode II, and 3.0 mL·h^{-1} for mode III. Overall, an identical behavior as the tensile tests was observed, where modifications made in the basic ES setup of mode I led to the production of stiffer scaffolds. A greater enhancement in the mechanical properties was achieved with the simultaneous electrospraying of PLGA/CIP NP as compared to the inclusion of CIP directly into the PEOT/PBT blend (Fig. 4B (i)). This was also confirmed by the significantly higher E values demonstrated by modes III (7.85 MPa) and IV
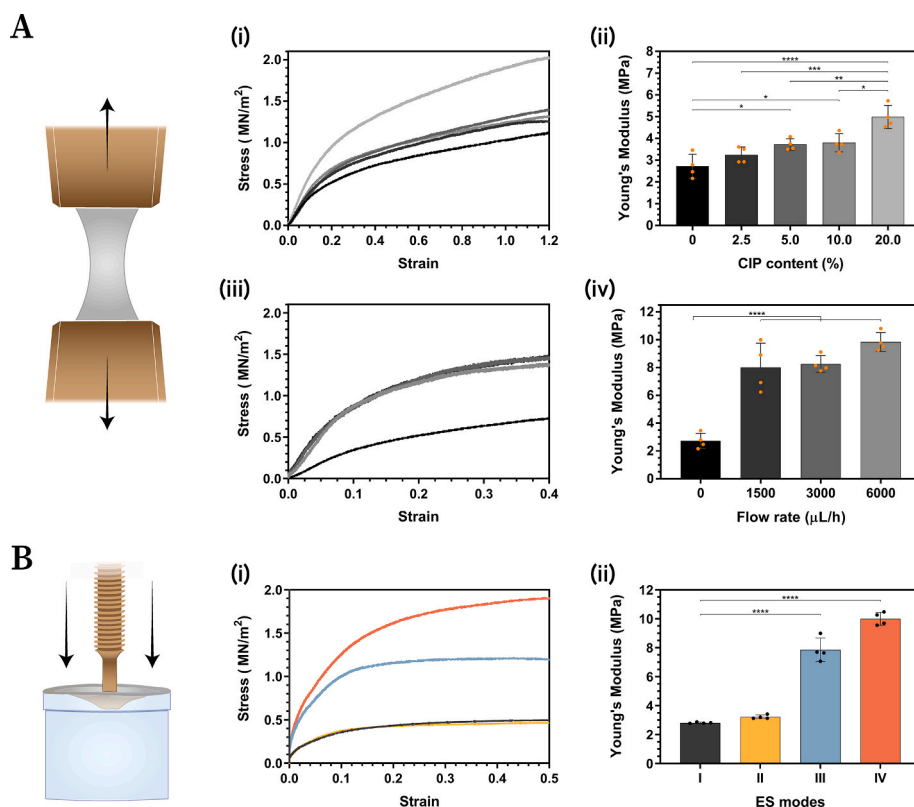
Fig. 4. Mechanical characterization of the electrospun patches. (A) Tensile measurement of mode II and III, presented by their corresponding stress-strain curves and Young's moduli ($n = 4$). **(B)** Indentation measurement of the best condition chosen for each mode (I–IV), presented by their corresponding stress-strain curves and Young's moduli ($n = 4$).

(9.99 MPa), in contrast to modes I (2.80 MPa) and II (3.22 MPa) (Fig. 4B (ii)). Moreover, considering that mode IV incorporated both blend ES and co-ES/electrospraying, it ultimately displayed the highest stiffness among all the modalities.

3.4. Biological characterization

A preliminary biocompatibility assessment of CIP was conducted on TCP using supplemented culture media (Figure S6A). No cytotoxic effects of the drug were detected on hMSCs up to a concentration of 33 µg·mL^{-1} (Figure S6B-C). Subsequently, the biological relevance of the implemented ES modalities was investigated with respect to the most optimal composition identified for each mode. Overall, all the TM scaffolds revealed an excellent viability and proliferation of the cultured hMSCs, yet several differences were noted across them in guiding the respective cellular responses.

Fig. 5A presents a qualitative demonstration of the cell distribution obtained on distinct substrates at the chosen timepoints. The cases with electrosprayed NP, in particular mode III, showed a lower cell attachment in comparison to the rest. This was further confirmed by the measurement of cell metabolic activity, with mode III exhibiting the lowest values at day 7 (Fig. 5B). However, no significant differences were detected between the samples at the earlier timepoints. Image quantification was performed to assess the influence of ES modality on cell coverage (Fig. 5C). Interestingly, scaffolds with the highest CIP concentration, that is mode II, displayed the maximum cell coverage (60.7 %), followed by modes I (43.7 %), IV (43.3 %), and III (41.9 %), respectively.

Following the successful evaluation of cell viability and coverage on the electrospun patches, the proliferative potential of the cultured hMSCs was investigated (Fig. 6A–C). Samples were stained for Ki-67, which is a nuclear protein expressed during all active phases of the

cell cycle (Fig. 6A and Figure S7). Qualitative analysis of the micrographs demonstrated a more pronounced presence of Ki-67-labelled nuclei on TCP as compared to the selected ES modalities. This was further verified through quantitative analysis of the captured images (Fig. 6C). Moreover, a comparable trend to the cell coverage was observed for the average dsDNA content, whereby scaffolds loaded with electrosprayed NP exhibited the lowest values (Fig. 6B).

3.5. Antibacterial validation

The antimicrobial validation of the electrospun patches was conducted using disk diffusion test and biofilm formation assay. Fig. 7A schematically illustrates the expected halo creation during the effective inhibition of bacterial growth. Under the tested conditions, the overall CIP concentration was identified as the most critical factor in inhibiting the growth of both *S. aureus* and *P. aeruginosa*. In this regard, mode II, with a cumulative release of 58 µg·mL^{-1}, and mode IV, with 21 µg·mL^{-1}, proved to be the only modalities with an evident inhibition halo (Figure S8). In contrast, mode I, which had no drug content, and mode III, with a cumulative concentration of 1 µg·mL^{-1}, exhibited no detectable antibacterial activity in this test. Fig. 7B presents a summary of the quantified halo diameters for each case.

The SEM analysis showed that the formation of the *S. aureus* biofilm was inhibited in all the samples, regardless of the presence of CIP (Fig. 7C). Conversely, for *P. aeruginosa*, sparse small clusters were observed in modes I, II, and IV, whereas a more extensive biofilm formation was evident solely in mode III.

The test carried with the crystal violet staining method showed a significant reduction in the ability to form biofilm for S. aureus in the presence of all meshes compared to the TCP control, which presented an optical density at 570/655 nm of approximately 3.0 (Figure S9). Furthermore, a reduction in biofilm formation was also obtained for P.
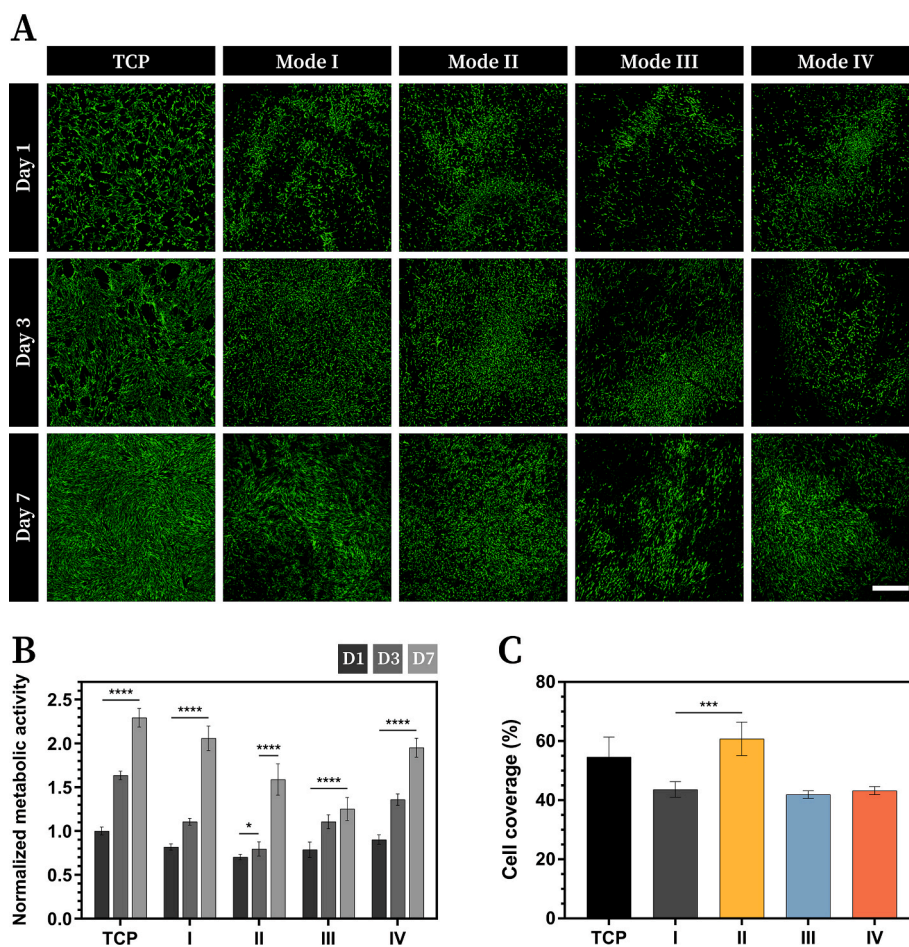
Fig. 5. Cell attachment and viability on the electrospun patches. (A) Live hMSCs (Calcein AM) imaged in green at days 1, 3, and 7, of culture on electrospun meshes and tissue culture plate (TCP). All images of this panel share the same scale bar, as indicated in the bottom right corner of the last image. The scale bar represents: 1000 μm. **(B)** Metabolic activity quantified with MTS assay at days 1, 3, and 7 ($n = 12$). All values have been normalized with respect to TCP on day 1. **(C)** Image quantification to determine the extent of cell coverage on electrospun scaffolds on day 1 ($n = 3$).

aeruginosa with respect to the TCP; however, with a lower efficiency, particularly in the case of mode III.

4. Discussion

CSOM ranks among the most widespread childhood infectious diseases across the globe [9]. Its exact etiology is yet to be completely understood, although it is believed to be a consequence of persistent middle ear inflammation resulting in a non-healing perforation of the TM [69]. Majority of the patients sustaining a long-standing episode of CSOM often end with a combined conductive and sensorineural hearing loss [70]. Therefore, multiple treatment strategies have been clinically tested for inhibiting the polymicrobial growth responsible for this chronic infection. These include systemic or topical use of antibiotics, topical antiseptics, and ear cleaning, which are routinely applied alone or in combination with each other [13,14,71,72]. In this regard, broad-spectrum otic fluoroquinolones, such as CIP, which have been approved by the EMA and FDA, have emerged as the primary first-line therapy for managing CSOM-induced otorrhea. Moreover, the topical application of the drug has been reported to be more effective in targeting the infected area as compared to the systemic approach [73]. In general, an antibiotic treatment for 7 days is sufficient to resolve most CSOM infections [14]; however, a personalized drug dosage and duration might be essential for avoiding any therapeutic complications [66].

Antibiotic therapy is increasingly becoming personalized, where a broad range of patient-specific factors need to be considered for deciding

an optimal dose [65]. These factors encompass patient characteristics, the site and severity of infection, pathogen susceptibility, as well as pharmacokinetic considerations. As a result, a patient-specific combination of ideal drug concentration, dosing frequency, and treatment duration is necessary to achieve the desired antimicrobial effect without the risks of overdosing. A minimum inhibitory concentration (MIC_{90}) of 3.0 μg·mL^{-1} has been identified adequate for CIP to suppress the growth of the most common pathogens isolated from chronic discharging ears, namely the Gram-negative bacterium, *P. aeruginosa*, and the Gram-positive bacterium, *S. aureus* [11,74]. However, CSOM patients are typically exposed to significantly higher dosages, with 1 mg per day in topical therapies and 1000 mg per day in systemic therapies [61,62], to compensate for the low drug penetration efficiency [75]. This is particularly true for cases with small TM perforations or copious ear discharge [14]. The use of elevated drug concentrations does ensure a robust treatment of the infected tissue but at the same time, is also accompanied by various antibiotic-associated risks. Several adverse effects of CIP overdose or prolonged administration have been reported in the literature, some of these include gastrointestinal distress, central nervous system disorders, tendinopathy, and in some rare cases, hepatotoxicity, nephrotoxicity, and cardiotoxicity [76]. Moreover, certain aminoglycoside antibiotics such as gentamicin, neomycin, and streptomycin are known to exhibit ototoxic effects, often resulting in drug-induced sensorineural hearing loss [77]. CIP, in this regard, is considered a comparatively safer drug, although studies have still indicated mild-to-moderate hair cell loss, predominantly within the
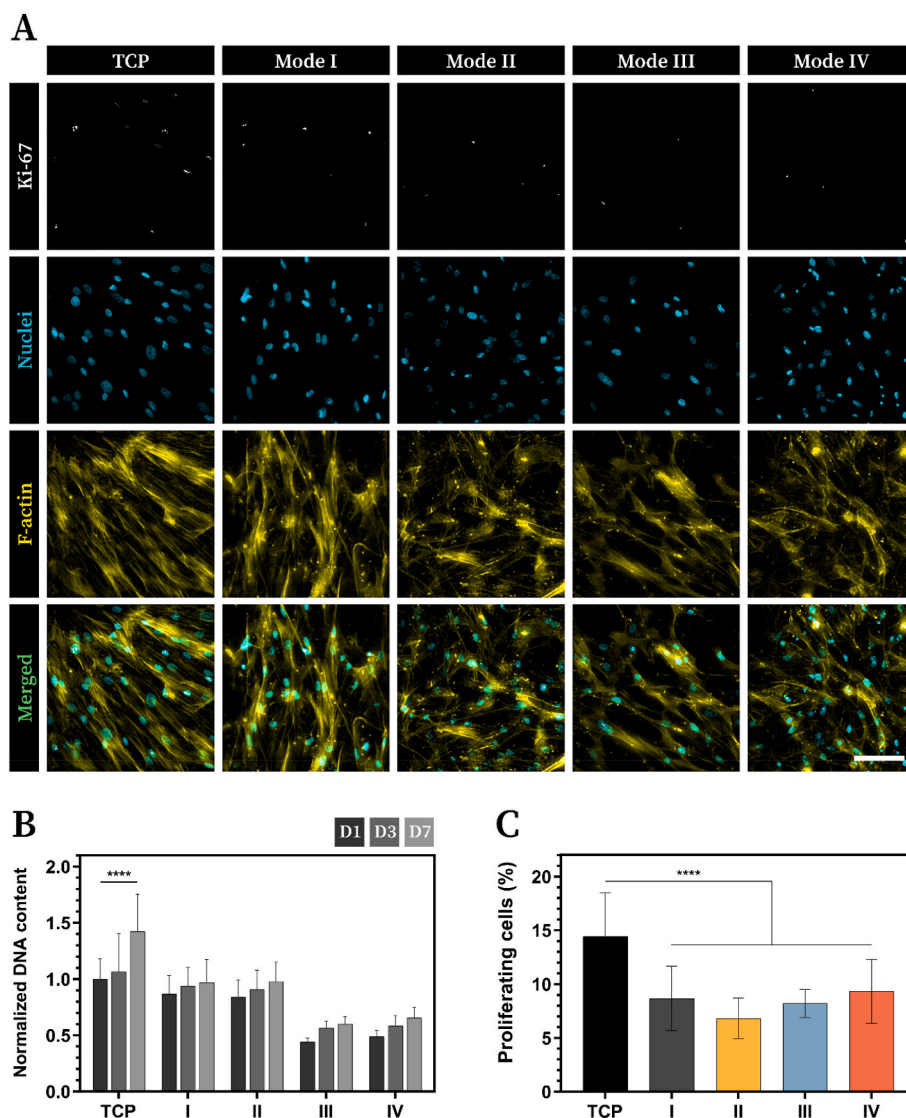
Fig. 6. Cell proliferation on the electrospun patches. (A) Immunofluorescence staining of the cultured hMSCs at day 3 to visualize Ki-67, a proliferation marker (white) along with the nuclei (cyan) and F-actin filaments (yellow). All images of this panel share the same scale bar, as indicated in the bottom right corner of the last image. The scale bar represents: 50 μm. **(B)** dsDNA quantification using PicoGreen assay at days 1, 3, and 7 ($n = 12$). All values have been normalized with respect to TCP on day 1. **(C)** Image quantification to determine the percentage of proliferating cells on day 7 ($n = 4$).

apical half of the cochlea [78].

Therefore, a targeted delivery of the antibiotic could prove beneficial in mitigating the complications associated with excessive exposure, without compromising its antimicrobial functionality. In addition, if this could be combined with the therapeutic approaches for patching the perforated TM, it could serve multiple purposes at once, thereby potentially reducing the clinical interventions required in the treatment of CSOM. With the recent advancement in biofabrication technologies, numerous drug loading strategies have been proposed and tested for the localized delivery of CIP. Among them, electrohydrodynamic techniques such as ES and electrospraying have emerged as promising approaches for achieving a controlled release of CIP from nanofibrous meshes over time [52,56–58]. However, no such procedure has yet been reported for the restoration of CSOM-induced TM perforations. Therefore, the current work aims at addressing this clinical gap by introducing structurally and mechanically relevant patches with tunable CIP loading and releasing characteristics to repair the infected eardrum.

Multiple ES modalities were investigated in this regard, to offer a broad range of release profiles and concentrations to cater to patient-specific antibiotic requirements. Each selected mode was individually

characterized to determine the optimal composition within it. This was performed with respect to an increasing CIP concentration in mode II and an increasing PLGA/CIP NP flow rate in mode III. Considering that the CIP concentration within the PLGA NP was kept consistent with the previously reported protocol [52], the NP flow rate was employed as the appropriate parameter to control the drug loading capacity in mode III. Overall, the morphological and physicochemical characterizations of the fabricated scaffolds confirmed successful incorporation of the antibiotic within all nanofibrous meshes. The FTIR and XRD spectra in mode II demonstrated an effective encapsulation of the drug inside the polymeric fibers. Moreover, a favorable influence of CIP was observed in reducing the fiber diameter and thickness for the blend electrospun compositions. This phenomenon could be attributed to the formation of positively charged CIP molecules, resulting in an enhanced stretching of the ES jet [79]. A similar protonation of amine groups was recently observed during the inclusion of chitin nanofibrils in the PEOT/PBT polymer solution, which yielded a three-fold reduction in the corresponding fiber diameters [36]. In the end, taking all these morphological and physicochemical characterizations into account, CIP 10.0 % was the most promising composition in mode II.
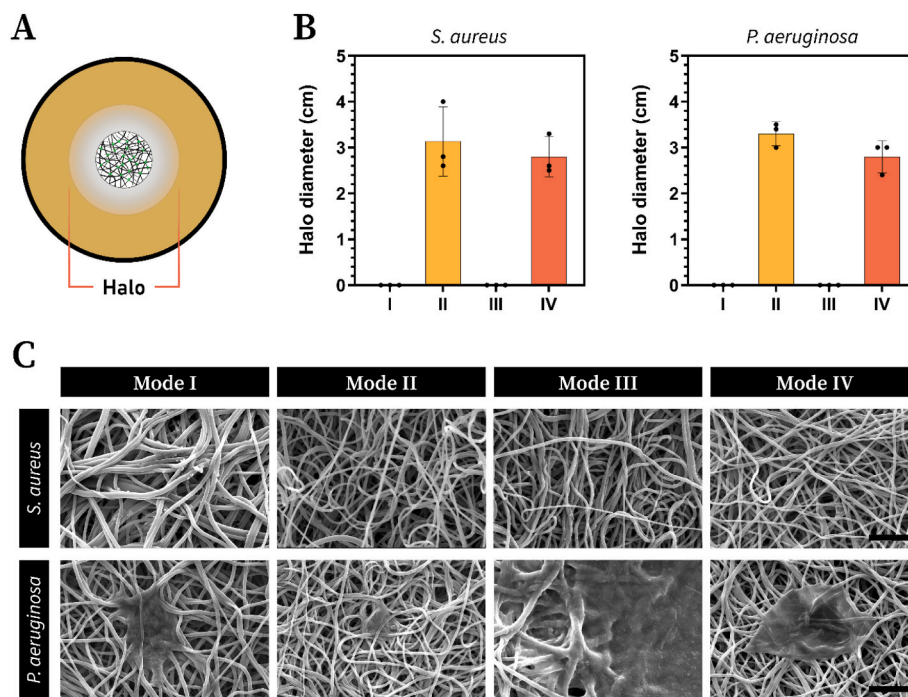
Fig. 7. Antibacterial validation of the electrospun patches. (A) Schematic representation of the inhibition halo created by the electrospun patches during disk diffusion tests. (B) Quantification of the halo diameter for S. aureus and P. aeruginosa ($n = 3$). (C) Biofilm assessment on the scaffold surface with respect to Gram-positive S. aureus and Gram-negative P. aeruginosa. All images of this panel share the same scale bar, as indicated in the bottom right corner of the last image. The scale bar represents: 10 μm.

On the other hand, in mode III, the electrosprayed PLGA/CIP NP did not seem to have a significant impact on the PEOT/PBT fiber diameters. However, they did on the fiber orientation and scaffold thickness. The increased curling of electrospun fibers at higher flow rates could be explained with respect to the decreasing surface tension of the collecting substrate. Considering the remarkably larger surface tension of aluminum as compared to water [80], the rise in the NP flow rate from 0 $mL \cdot h^{-1}$ to 6.0 $mL \cdot h^{-1}$ is associated to a gradual decline in their subsequent surface tension. Literature suggests a dominant role of the collector's surface tension in guiding the morphology of the deposited fibers [81]. The current study provided the first validation of this phenomenon for PEOT/PBT, using wet ES as a positive control. In this regard, a lower surface tension was noted to disperse the fibers more readily, thereby inducing a higher curling effect [81]. Furthermore, this increase in fiber dispersion also justifies the decrease in scaffold thickness. To conclude, the morphological differences between the CIP-loaded scaffolds of mode III were not as drastic as in mode II; however, amidst the minor variations, the flow rate of 3.0 $mL \cdot h^{-1}$ was the most optimal condition.

Following the successful fabrication of the CIP-loaded electrospun scaffolds, the release of their corresponding drug cargo was quantified. In general, the mode II meshes could be applicable for CSOM cases demanding a higher and longer antibiotic treatment, whereas the mode III ones could be suitable for smaller and shorter dosages. Three distinct stages of drug release have been reported in the literature for blend electrospun fibers [59]. Stage I is governed by Fick's second law, where the swelling of fibers controls the diffusion through them. Stage II is dominated by diffusion too, although through a fused membrane structure. Finally, in stage III, the polymer degradation takes over and releases the remaining drug. A similar mechanism involving a combination of diffusion, swelling, and degradation has also been observed during the drug release from PLGA NP [82]. However, considering the underlying difference in the chemical breakdown of PEOT/PBT and PLGA in aqueous solutions [36,83], the CIP release kinetics obtained due to them is quite contrasting. Moreover, in case of mode II, even the

methodology of preparing the PEOT/PBT/CIP blends was noticed to influence the release mechanism, and subsequently the overall kinetics. Scaffolds fabricated after an US step revealed a burst release in comparison to those produced without it. This was attributed to the entrapment of the drug within the polymer network when the precursor solution was not ultrasonicated (US-). Overall, the Weibull model of drug release kinetics was chosen as the fitting mathematical model for the investigated TM patches. The flexibility of the Weibull model allows it to cover a wide range of release profiles, thereby explaining the diverse kinetics obtained with the different fabrication modalities in this study [84].

Previous studies have highlighted the role of mechanical properties in the creation of biomimetic TM replacements [19,36]. In this regard, tensile and indentation measurements were carried out to validate the mechanical performance of the CIP loaded scaffolds. The macro-indentation approach is a useful tool for evaluating the scaffold functionality, taking the anisotropic behavior of the native TM into account [85]. Overall, the incorporation of CIP either through blend ES or co-ES/electrospraying was noted to enhance the mechanical properties of PEOT/PBT-based TM patches. This enhancement aligns with multiple studies in the past, where nanofillers or geometrical features were utilized to achieve similar reinforcement of electrospun meshes [19,36]. Among the investigated compositions, CIP concentration of 20.0 % in mode II and NP flow rate of 6.0 $mL \cdot h^{-1}$ in mode III demonstrated significantly higher E values as compared to their counterparts. This observation can be attributed to the appearance of beads with increasing drug concentration and greater fiber curling with a rising flow rate.

Given the increasing importance of hMSCs in TM regeneration [86], they were chosen as the appropriate cell type for this study. The *in vitro* experiments conducted on the electrospun patches revealed a consistent cell attachment, viability, and proliferation across all the tested samples. Ultimately, the antibacterial studies confirmed the efficacy of the presented CIP release model in inhibiting bacterial growth. The bacterial strains of *S. aureus* and *P. aeruginosa*, being the most commonly isolated pathogens during CSOM [11], were applied in this regard. In general,

the ES modalities involving the blend component, namely modes II and IV, were found to be more effective. This suggests that the CIP concentration achieved with mode III may not be sufficient to counteract an active, severe infection. To further strengthen the outcomes of the disk diffusion test, the fabricated meshes underwent a biofilm formation assay. All TM scaffolds exhibited the ability to inhibit the formation of biofilm in the case of *S. aureus*. However, for *P. aeruginosa*, while the biofilm formation was significantly inhibited in modes II and IV, a substantial presence was detected in mode III, thus corroborating the previous results of the inhibition halo.

5. Conclusion

This work addresses the current clinical gap in the availability of functional TM patches possessing tunable antibiotic releasing capabilities. It presents an innovative therapeutic solution that synergistically combines tissue engineering with drug delivery, with the aim of minimizing clinical intervention in the treatment of CSOM-induced TM perforations. In this regard, four distinct ES modalities were implemented and investigated in terms of their morphological, physicochemical, mechanical, biological, drug releasing, and antibacterial responses. The modified ES setups (modes II, III, and IV) allowed a successful incorporation of CIP while introducing distinct morphological features within the resultant electrospun fibers, as compared to the control (mode I). A positive impact of these variations was observed with respect to their corresponding mechanical properties, where the CIP-loaded scaffolds exhibited a reinforced response. Furthermore, the chosen modalities highlighted the possibility to fabricate TM patches with patient-specific antibiotic requirements. Among them, the blend ES approach (mode II) was carefully optimized to yield a sustained release of CIP for 7 days. On the other hand, a faster delivery rate was demonstrated with the simultaneous electrospraying of PLGA/CIP NP. *In vitro* antibacterial validations performed with gram-positive and gram-negative bacteria assessed the efficacy of different drug-loading modalities in suppressing the bacterial infection. Considering the high loading concentration used for blend ES, a greater inhibition of bacterial growth was reported for modes II and IV. Finally, the biological relevance of this study was verified by showing that the amount of CIP released from each mode did not show any cytotoxic and antiproliferative effects on the cultured hMSCs. Future work will be focused on applying these antibiotic-laden TM patches in an animal model to evaluate their overall effectiveness *in vivo*.

6. Ethics approval and consent to participate

Ethical approval was obtained from the local and national authorities to isolate human mesenchymal stromal cells from the iliac crest (Donor 064, male, age 17, Maastricht University Medical Center, Maastricht, the Netherlands). All procedures were carried out in accordance with the World Medical Association Declaration of Helsinki in its latest amendment.

All authors have confirmed the contents of the manuscript and approved its submission for publication.

Funding

The authors thank Mr. Victor Sarrucco, Ms. Julie Tenwolde, Mr. Yonis al Tammar, and Ms. Agnieszka Talik (BBS3004 students at Maastricht University, the Netherlands) for their assistance with the quantification of biological data.

CRediT authorship contribution statement

Shivesh Anand: Writing – original draft, Validation, Methodology, Investigation, Formal analysis, Data curation, Conceptualization. **Alessandra Fusco:** Validation, Methodology, Investigation, Formal analysis.

Cemre Günday: Investigation. **Nazende Günday Türeli:** Supervision, Methodology, Funding acquisition. **Giovanna Donnarumma:** Validation, Supervision, Methodology. **Serena Danti:** Writing – review & editing, Funding acquisition. **Lorenzo Moroni:** Writing – review & editing, Supervision, Resources, Funding acquisition. **Carlos Mota:** Conceptualization, Funding acquisition, Resources, Supervision, Writing – review & editing.

Declaration of Competing interest

The authors declare no conflict of interest.

Acknowledgements

Appendix A. Supplementary data

Supplementary data to this article can be found online at https://doi.org/10.1016/j.bioactmat.2024.04.001.

References

[1] J.M. Hempel, A. Becker, J. Müller, E. Krause, A. Berghaus, T. Braun, Traumatic tympanic membrane perforations: clinical and audiometric findings in 198 patients, Otol. Neurotol. 33 (8) (2012) 1357–1362.

[2] J. Isaacson, N.M. Vora, Differential diagnosis and treatment of hearing loss, Am. Fam. Physician 68 (6) (2003) 1125–1132.

[3] L. Monasta, L. Ronfani, F. Marchetti, M. Montico, L. Vecchi Brumatti, A. Bavcar, D. Grasso, C. Barbiero, G. Tamburlini, Burden of disease caused by otitis media: systematic review and global estimates, PLoS One 7 (4) (2012) e36226.

[4] A.G. Schilder, T. Chonmaitree, A.W. Cripps, R.M. Rosenfeld, M.L. Casselbrant, M. P. Haggard, R.P. Venekamp, Otitis media, Nat. Rev. Dis. Prim. 2 (1) (2016) 1–18.

[5] K.A. Cullen, M.J. Hall, A. Golosinskiy, Ambulatory Surgery in the United States, 2006, 2009.

[6] M. Gulliford, R. Latinovic, J. Charlton, P. Little, T. van Staa, M. Ashworth, Selective decrease in consultations and antibiotic prescribing for acute respiratory tract infections in UK primary care up to 2006, Journal of public health 31 (4) (2009) 512–520.

[7] A.J. Leach, P.S. Morris, Antibiotics for the prevention of acute and chronic suppurative otitis media in children, Cochrane Database Syst. Rev. (4) (2006).

[8] J.O. Hendley, Otitis media, N. Engl. J. Med. 347 (15) (2002) 1169–1174.

[9] M. Verhoeff, E.L. van der Veen, M.M. Rovers, E.A. Sanders, A.G. Schilder, Chronic suppurative otitis media: a review, Int. J. Pediatr. Otorhinolaryngol. 70 (1) (2006) 1–12.

[10] R. Prakash, D. Juyal, V. Negi, S. Pal, S. Adekhandi, M. Sharma, N. Sharma, Microbiology of chronic suppurative otitis media in a tertiary care setup of Uttarakhand state, India, N. Am. J. Med. Sci. 5 (4) (2013) 282.

[11] W.N.A. Wan Draman, M.K. Md Daud, H. Mohamad, S.A. Hassan, N. Abd Rahman, Evaluation of the current bacteriological profile and antibiotic sensitivity pattern in chronic suppurative otitis media, Laryngoscope investigative otolaryngology 6 (6) (2021) 1300–1306.

[12] S. Saini, N. Gupta, O. Sachdeva, Bacteriological study of paediatric and adult chronic suppurative otitis media, Indian J. Pathol. Microbiol. 48 (3) (2005) 413–416.

[13] L.-Y. Chong, K. Head, K.E. Webster, J. Daw, P. Richmond, T. Snelling, M.F. Bhutta, A.G. Schilder, M.J. Burton, C.G. Brennan-Jones, Systemic antibiotics for chronic suppurative otitis media, Cochrane Database Syst. Rev. 2 (2021).

[14] C.G. Brennan-Jones, K. Head, L.Y. Chong, M.J. Burton, A.G. Schilder, M.F. Bhutta, Topical antibiotics for chronic suppurative otitis media, Cochrane Database Syst. Rev. 1 (2020).

[15] R. Indudharan, J.A. Haq, S. Aiyar, Antibiotics in chronic suppurative otitis media: a bacteriologic study, Ann. Otol. Rhinol. Laryngol. 108 (5) (1999) 440–445.

[16] S. Kanth, Y. Malgar Puttaiahgowda, S. Gupta, Recent advancements and perspective of ciprofloxacin-based antimicrobial polymers, J. Biomater. Sci. Polym. Ed. 34 (7) (2023) 918–949.

[17] C.A. Macfadyen, J.M. Acuin, C.L. Gamble, Topical antibiotics without steroids for chronically discharging ears with underlying eardrum perforations, Cochrane Database Syst. Rev. (4) (2005).

[18] P.L.S. Maria, J.S. Oghalai, Is office-based myringoplasty a suitable alternative to surgical tympanoplasty? Laryngoscope 124 (5) (2014) 1053–1054.

[19] S. Anand, T. Stoppe, M. Lucena, T. Rademakers, M. Neudert, S. Danti, L. Moroni, C. Mota, Mimicking the human tympanic membrane: the significance of scaffold geometry, Adv. Healthcare Mater. 10 (11) (2021) 2002082.

[20] M. von Witzleben, T. Stoppe, T. Ahlfeld, A. Bernhardt, M.L. Polk, M. Bornitz, M. Neudert, M. Gelinsky, Biomimetic tympanic membrane replacement made by melt electrowriting, Adv. Healthcare Mater. 10 (10) (2021) 2002089.

[21] C.H. Jang, S. Ahn, J.W. Lee, B.H. Lee, H. Lee, G. Kim, Mesenchymal stem cell-laden hybrid scaffold for regenerating subacute tympanic membrane perforation, Mater. Sci. Eng. C 72 (2017) 456–463.

[22] M. Aleemardani, Z. Bagher, M. Farhadi, H. Chahsetareh, R. Najafi, B. Eftekhari, A. Seifalian, Can tissue engineering bring hope to the development of human tympanic membrane? Tissue Engineering Part B: Reviews 27 (6) (2021) 572–589.

[23] X. Zhao, J. Zhang, P. Tian, X. Cui, The latest progress of tympanic membrane repair materials, Am. J. Otolaryngol. 43 (5) (2022) 103408.

[24] R. Ghassemifar, S. RedmondZainuddin, T.V. Chirila, Advancing towards a tissue-engineered tympanic membrane: silk fibroin as a substratum for growing human eardrum keratinocytes, J. Biomater. Appl. 24 (7) (2010) 591–606.

[25] B. Levin, S.L. Redmond, R. Rajkhowa, R.H. Eikelboom, M.D. Atlas, R.J. Marano, Utilising silk fibroin membranes as scaffolds for the growth of tympanic membrane keratinocytes, and application to myringoplasty surgery, J. Laryngol. Otol. 127 (Suppl 1) (2013) S13–S20.

[26] D.E. Weber, M.T. Semaan, J.K. Wasman, R. Beane, L.J. Bonassar, C.A. Megerian, Tissue-engineered calcium alginate patches in the repair of chronic chinchilla tympanic membrane perforations, Laryngoscope 116 (5) (2006) 700–704.

[27] Z.C. Lou, J.G. He, A randomised controlled trial comparing spontaneous healing, gelfoam patching and edge-approximation plus gelfoam patching in traumatic tympanic membrane perforation with inverted or everted edges, Clinical otolaryngology : official journal of ENT-UK ; official journal of Netherlands Society for Oto-Rhino-Laryngology & Cervico-Facial Surgery 36 (3) (2011) 221–226.

[28] C.Y. Kuo, E. Wilson, A. Fuson, N. Gandhi, R. Monfaredi, A. Jenkins, M. Romero, M. Santoro, J.P. Fisher, K. Cleary, B. Reilly, Repair of tympanic membrane perforations with customized bioprinted ear grafts using Chinchilla models, tissue engineering, Part A 24 (5–6) (2018) 527–535.

[29] E.D. Kozin, N.L. Black, J.T. Cheng, M.J. Cotler, M.J. McKenna, D.J. Lee, J.A. Lewis, J.J. Rosowski, A.K. Remenschneider, Design, fabrication, and in vitro testing of novel three-dimensionally printed tympanic membrane grafts, Hear. Res. 340 (2016) 191–203.

[30] H. Lee, C.H. Jang, G.H. Kim, A polycaprolactone/silk-fibroin nanofibrous composite combined with human umbilical cord serum for subacute tympanic membrane perforation; an in vitro and in vivo study, J. Mater. Chem. B 2 (18) (2014) 2703–2713.

[31] H. Seonwoo, B. Shin, K.J. Jang, M. Lee, O.S. Choo, S.B. Park, Y.C. Kim, M.J. Choi, J. Kim, P. Garg, J.H. Jang, Epidermal growth factor–releasing radially aligned electrospun nanofibrous patches for the regeneration of chronic tympanic membrane perforations, Adv. Healthcare Mater. 8 (2) (2019) 1801160.

[32] S. Moscato, A. Rocca, D. D'Alessandro, D. Puppi, V. Gramigna, M. Milazzo, C. Stefanini, F. Chiellini, M. Petrini, S. Berrettini, S. Danti, Tympanic membrane collagen expression by dynamically cultured human mesenchymal stromal cell/star-branched poly(ε-caprolactone) nonwoven constructs, Appl. Sci. 10 (9) (2020) 3043.

[33] C. Mota, S. Danti, D. D'Alessandro, L. Trombi, C. Ricci, D. Puppi, D. Dinucci, M. Milazzo, C. Stefanini, F. Chiellini, L. Moroni, S. Berrettini, Multiscale fabrication of biomimetic scaffolds for tympanic membrane tissue engineering, Biofabrication 7 (2) (2015) 025005.

[34] S. Danti, C. Mota, D. D'alessandro, L. Trombi, C. Ricci, S.L. Redmond, A. De Vito, R. Pini, R.J. Dilley, L. Moroni, S. Berrettini, Tissue engineering of the tympanic membrane using electrospun PEOT/PBT copolymer scaffolds: a morphological in vitro study, Hear. Bal. Commun. 13 (4) (2015) 133–147.

[35] S. Danti, S. Anand, B. Azimi, M. Milazzo, A. Fusco, C. Ricci, L. Zavagna, S. Linari, G. Donnarumma, A. Lazzeri, Chitin nanofibril application in tympanic membrane scaffolds to modulate inflammatory and immune response, Pharmaceutics 13 (9) (2021) 1440.

[36] S. Anand, B. Azimi, M. Lucena, C. Ricci, M. Candito, L. Zavagna, L. Astolfi, M.-B. Coltelli, A. Lazzeri, S. Berrettini, Chitin nanofibrils modulate mechanical response in tympanic membrane replacements, Carbohydrate Polymers 310 (2023) 120732.

[37] A.P.S. Immich, P.C. Pennacchi, A.F. Naves, S.L. Felisbino, R.L. Boemo, S.S. Maria-Engler, L.H. Catalani, Improved tympanic membrane regeneration after myringoplastic surgery using an artificial biograft, Mater Sci Eng C Mater Biol Appl 73 (2017) 48–58.

[38] L. Li, W. Zhang, M. Huang, J. Li, J. Chen, M. Zhou, J. He, Preparation of gelatin/genipin nanofibrous membrane for tympanic member repair, Journal of biomaterials science 29 (17) (2018). Polymer edition.

[39] B. Wang, T. Xin, L. Shen, K. Zhang, D. Zhang, H. Zhang, J. Liu, B. Chen, W. Cui, Y. Shu, Acoustic transmitted electrospun fibrous membranes for tympanic membrane regeneration, Chem. Eng. J. 419 (2021) 129536.

[40] L. Benecke, Z. Chen, I. Zeidler-Rentzsch, M. von Witzleben, M. Bornitz, T. Zahnert, M. Neudert, C. Cherif, D. Aibibu, Development of electrospun, biomimetic tympanic membrane implants with tunable mechanical and oscillatory properties for myringoplasty, Biomater. Sci. 10 (9) (2022) 2287–2301.

[41] E. Ilhan, S. Ulag, A. Sahin, B.K. Yilmaz, N. Ekren, O. Kilic, M. Sengor, D. M. Kalaskar, F.N. Oktar, O. Gunduz, Fabrication of tissue-engineered tympanic membrane patches using 3D-Printing technology, J. Mech. Behav. Biomed. Mater. 114 (2021) 104219.

[42] A.A. Rostam-Alilou, H. Jafari, A. Zolfagharian, A. Serjouei, M. Bodaghi, Experimentally validated vibro-acoustic modeling of 3D bio-printed grafts for potential use in human tympanic membrane regeneration, Bioprinting 25 (2022) e00186.

[43] W.E. Teo, S. Ramakrishna, A review on electrospinning design and nanofibre assemblies, Nanotechnology 17 (14) (2006) R89.

[44] T.J. Sill, H.A. Von Recum, Electrospinning: applications in drug delivery and tissue engineering, Biomaterials 29 (13) (2008) 1989–2006.

[45] X. Hu, S. Liu, G. Zhou, Y. Huang, Z. Xie, X. Jing, Electrospinning of polymeric nanofibers for drug delivery applications, J. Contr. Release 185 (2014) 12–21.

[46] S.E. Gilchrist, D. Lange, K. Letchford, H. Bach, L. Fazli, H.M. Burt, Fusidic acid and rifampicin co-loaded PLGA nanofibers for the prevention of orthopedic implant associated infections, J. Contr. Release 170 (1) (2013) 64–73.

[47] P.G. Shikhi-Abadi, M. Irani, A review on the applications of electrospun chitosan nanofibers for the cancer treatment, Int. J. Biol. Macromol. 183 (2021) 790–810.

[48] S.Y. Chew, J. Wen, E.K. Yim, K.W. Leong, Sustained release of proteins from electrospun biodegradable fibers, Biomacromolecules 6 (4) (2005) 2017–2024.

[49] Y. Luu, K. Kim, B. Hsiao, B. Chu, M. Hadjiargyrou, Development of a nanostructured DNA delivery scaffold via electrospinning of PLGA and PLA–PEG block copolymers, J. Contr. Release 89 (2) (2003) 341–353.

[50] P.-o. Rujitanaroj, Y.-C. Wang, J. Wang, S.Y. Chew, Nanofiber-mediated controlled release of siRNA complexes for long term gene-silencing applications, Biomaterials 32 (25) (2011) 5915–5923.

[51] M.E. Wright, I.C. Parrag, M. Yang, J.P. Santerre, Electrospun polyurethane nanofiber scaffolds with ciprofloxacin oligomer versus free ciprofloxacin: effect on drug release and cell attachment, J. Contr. Release 250 (2017) 107–115.

[52] C. Günday, S. Anand, H.B. Gencer, S. Munafò, L. Moroni, A. Fusco, G. Donnarumma, C. Ricci, P.C. Hatir, N.G. Türeli, A.E. Türeli, C. Mota, S. Danti, Ciprofloxacin-loaded polymeric nanoparticles incorporated electrospun fibers for drug delivery in tissue engineering applications, Drug delivery and translational research 10 (3) (2020).

[53] J. Yang, K. Wang, D.-G. Yu, Y. Yang, S.W.A. Bligh, G.R. Williams, Electrospun Janus nanofibers loaded with a drug and inorganic nanoparticles as an effective antibacterial wound dressing, Mater. Sci. Eng. C 111 (2020) 110805.

[54] P. Heydari, A. Zargar Kharazi, S. Asgary, S. Parham, Comparing the wound healing effect of a controlled release wound dressing containing curcumin/ciprofloxacin and simvastatin/ciprofloxacin in a rat model: a preclinical study, J. Biomed. Mater. Res. 110 (2) (2022) 341–352.

[55] A.M. Moydeen, M.S.A. Padusha, B.M. Thamer, A.M. Al-Enizi, H. El-Hamshary, M. H. El-Newehy, Single-nozzle core-shell electrospun nanofibers of pvp/dextran as drug delivery system, Fibers Polym. 20 (10) (2019) 2078–2089.

[56] S. Zupancic, S. Sinha-Ray, S. Sinha-Ray, J. Kristl, A.L. Yarin, Long-term sustained ciprofloxacin release from PMMA and hydrophilic polymer blended nanofibers, Mol. Pharm. 13 (1) (2016) 295–305.

[57] Z. Zhang, J. Tang, H. Wang, Q. Xia, S. Xu, C.C. Han, Controlled antibiotics release system through simple blended electrospun fibers for sustained antibacterial effects, ACS Appl. Mater. Interfaces 7 (48) (2015) 26400–26404.

[58] R. Elashnikov, S. Rimpelová, O. Lyutakov, V.r.S. Pavlíčková, O. Khrystonko, Z. k. Kolská, V.c. Švorčík, Ciprofloxacin-loaded poly (N-isopropylacrylamide-co-acrylamide)/Polycaprolactone nanofibers as dual thermo-and pH-responsive antibacterial materials, ACS Appl. Bio Mater. 5 (4) (2022) 1700–1709.

[59] J. Wu, Z. Zhang, W. Zhou, X. Liang, G. Zhou, C.C. Han, S. Xu, Y. Liu, Mechanism of a long-term controlled drug release system based on simple blended electrospun fibers, J. Contr. Release 320 (2020) 337–346.

[60] G.S. Shaw, S. Samavedi, Potent particle-based vehicles for growth factor delivery from electrospun meshes: fabrication and functionalization strategies for effective tissue regeneration, ACS Biomater. Sci. Eng. 8 (1) (2021) 1–15.

[61] A.V. Gurov, A.I. Kriukov, V.Y. Kunelskaya, G.N. Isotova, G.B. Shadrin, Y. V. Luchsheva, V.O. Yakimov, A. Garg, S.P. Akku, N. Gupta, Evaluation of the efficacy and tolerability of oral ciprofloxacin used in the comprehensive treatment of external bacterial otitis: an observational prospective study, Int. Arch. Otorhinolaryngol. 21 (2017) 329–335.

[62] R. Mösges, M. Nematian-Samani, A. Eichel, Treatment of acute otitis externa with ciprofloxacin otic 0.2% antibiotic ear solution, Therapeut. Clin. Risk Manag. (2011) 325–336.

[63] G.A. O'Toole, R. Kolter, Initiation of biofilm formation in Pseudomonas fluorescens WCS365 proceeds via multiple, convergent signalling pathways: a genetic analysis, Mol. Microbiol. 28 (3) (1998) 449–461.

[64] M. Abroodi, A. Bagheri, B.M. Razavizadeh, Surface tension of binary and ternary systems containing monoethanolamine (MEA), water and alcohols (methanol, ethanol, and isopropanol) at 303.15 K, J. Chem. Eng. Data 65 (6) (2020) 3173–3182.

[65] C. Moser, C.J. Lerche, K. Thomsen, T. Hartvig, J. Schierbeck, P.Ø. Jensen, O. Ciofu, N. Høiby, Antibiotic therapy as personalized medicine–general considerations and complicating factors, Apmis 127 (5) (2019) 361–371.

[66] R.J. Ruben, Otitis media: the application of personalized medicine, Otolaryngology-Head Neck Surg. (Tokyo) 145 (5) (2011) 707–712.

[67] F. Sisto, A. Bonomi, L. Cavicchini, V. Coccè, M.M. Scaltrito, G. Bondiolotti, G. Alessandri, E. Parati, A. Pessina, Human mesenchymal stromal cells can uptake and release ciprofloxacin, acquiring in vitro anti-bacterial activity, Cytotherapy 16 (2) (2014) 181–190.

[68] S. Anand, S. Danti, L. Moroni, C. Mota, Regenerative therapies for tympanic membrane, Prog. Mater. Sci. (2022) 100942.

[69] M.F. Bhutta, R.B. Thornton, L.-A.S. Kirkham, J.E. Kerschner, M.T. Cheeseman, Understanding the aetiology and resolution of chronic otitis media from animal and human studies, Disease models & mechanisms 10 (11) (2017) 1289–1300.

[70] T. Deitmer, Topical and systemic treatment for chronic suppurative otitis media, Ear, Nose and Throat Journal 81 (8) (2002). S16-S16.

[71] K. Head, L.-Y. Chong, M.F. Bhutta, P.S. Morris, S. Vijayasekaran, M.J. Burton, A. G. Schilder, C.G. Brennan-Jones, Antibiotics versus topical antiseptics for chronic suppurative otitis media, Cochrane Database Syst. Rev. (1) (2020).

[72] M.F. Bhutta, K. Head, L.-Y. Chong, J. Daw, A.G. Schilder, M.J. Burton, C. G. Brennan-Jones, Aural toilet (ear cleaning) for chronic suppurative otitis media, Cochrane Database Syst. Rev. 9 (2020).

[73] P.S. Roland, Ototopical agents are superior to systemic therapy for the treatment of acute and chronic otitis media, Ear, nose & throat journal 83 (9_suppl_4) (2004) 9–12.

[74] H. Sueke, S. Kaye, T. Neal, C. Murphy, A. Hall, D. Whittaker, S. Tuft, C. Parry, Minimum inhibitory concentrations of standard and novel antimicrobials for isolates from bacterial keratitis, Investigative ophthalmology & visual science 51 (5) (2010) 2519–2524.

[75] G. Delage, F. Boucher, H. Davies, J. Embree, C. Morin, D. Speert, B. Tan, High dose amoxicillin: rationale for use in otitis media treatment failures, Can. J. Infect Dis. 10 (4) (1999) 277–278.

[76] S. Badawy, Y. Yang, Y. Liu, M.A. Marawan, I. Ares, M.-A. Martinez, M.-R. Martínez-Larrañaga, X. Wang, A. Anadón, M. Martínez, Toxicity induced by ciprofloxacin and enrofloxacin: oxidative stress and metabolism, Crit. Rev. Toxicol. 51 (9) (2021) 754–787.

[77] J. Guo, R. Chai, H. Li, S. Sun, Protection of hair cells from ototoxic drug-induced hearing loss, Hear. Loss: Mechanisms, prevention and cure (2019) 17–36.

[78] A.L. Edmunds, Otiprio: an FDA-approved ciprofloxacin suspension gel for pediatric otitis media with effusion, Pharmacy and Therapeutics 42 (5) (2017) 307.

[79] E. Dos Santos, Z. Rozynek, E.L. Hansen, R. Hartmann-Petersen, R. Klitgaard, A. Løbner-Olesen, L. Michels, A. Mikkelsen, T.S. Plivelic, H. Bordallo, Ciprofloxacin intercalated in fluorohectorite clay: identical pure drug activity and toxicity with higher adsorption and controlled release rate, RSC advances 7 (43) (2017) 26537–26545.

[80] I.F. Bainbridge, J.A. Taylor, The surface tension of pure aluminum and aluminum alloys, Metall. Mater. Trans. 44 (2013) 3901–3909.

[81] M.B. Taskin, L.H. Klausen, M. Dong, M. Chen, Emerging wet electrohydrodynamic approaches for versatile bioactive 3D interfaces, Nano Res. 13 (2020) 315–327.

[82] D.J. Hines, D.L. Kaplan, Poly (lactic-co-glycolic) acid− controlled-release systems: experimental and modeling insights, Critical Reviews™ in Therapeutic Drug Carrier Systems 30 (3) (2013).

[83] H.K. Makadia, S.J. Siegel, Poly lactic-co-glycolic acid (PLGA) as biodegradable controlled drug delivery carrier, Polymers 3 (3) (2011) 1377–1397.

[84] S. Dash, P.N. Murthy, L. Nath, P. Chowdhury, Kinetic modeling on drug release from controlled drug delivery systems, Acta Pol. Pharm. 67 (3) (2010) 217–223.

[85] K. Williams, A. Blayney, T. Lesser, Mode shapes of a damaged and repaired tympanic membrane as analysed by the finite element method, Clinical Otolaryngology & Allied Sciences 22 (2) (1997) 126–131.

[86] N. Maharajan, G.W. Cho, C.H. Jang, Application of mesenchymal stem cell for tympanic membrane regeneration by tissue engineering approach, Int. J. Pediatr. Otorhinolaryngol. 133 (2020) 109969.